Received: 11 April 2023 | Revised: 28 December 2023 | Accepted: 20 March 2024

DOI: 10.1002/mp.17065

RESEARCH ARTICLE

MEDICAL PHYSICS

An essentially radiation-transparent body coil integrated with a patient rotation system for MR-guided particle therapy

Kilian A. Dietrich[1,2,3,4] | **Sebastian Klüter**[1,5,6] | **Fabian Dinkel**[6,7] | **Gernot Echner**[6,7] | **Stephan Brons**[8] | **Stephan Orzada**[1,2] | **Jürgen Debus**[1,3,4,5,6,8,9,10,11] | **Mark E. Ladd**[2,3,11] | **Tanja Platt**[1,2,4]

[1]Department of Radiation Oncology, Heidelberg University Hospital, Heidelberg, Germany

[2]Medical Physics in Radiology, German Cancer Research Center (DKFZ), Heidelberg, Germany

[3]Faculty of Physics, Heidelberg University, Heidelberg, Germany

[4]Clinical Cooperation Unit Radiation Oncology, German Cancer Research Center (DKFZ), Heidelberg, Germany

[5]National Center for Radiation Research in Oncology (NCRO), Heidelberg, Germany

[6]Heidelberg Institute of Radiation Oncology (HIRO), Heidelberg, Germany

[7]Division of Medical Physics in Radiation Oncology, German Cancer Research Center (DKFZ), Heidelberg, Germany

[8]Heidelberg Ion-Beam Therapy Center (HIT), Heidelberg University Hospital, Heidelberg, Germany

[9]German Cancer Consortium (DKTK), Heidelberg, Germany

[10]National Center for Tumor Diseases (NCT), Heidelberg, Germany

[11]Faculty of Medicine, Heidelberg University, Heidelberg, Germany

Correspondence
Kilian A. Dietrich, Department of Radiation Oncology, Heidelberg University Hospital, Heidelberg, Germany.
Postal address: Deutsches Krebsforschungszentrum (DKFZ), Im Neuenheimer Feld 280, 69120 Heidelberg, Germany.
Email: kilian.dietrich@dkfz-heidelberg.de

Funding information
German Federal Ministry of Education and Research, Grant/Award Number: 13GW0436

Abstract

Background: The pursuit of adaptive radiotherapy using MR imaging for better precision in patient positioning puts stringent demands on the hardware components of the MR scanner. Particularly in particle therapy, the dose distribution and thus the efficacy of the treatment is susceptible to beam attenuation from interfering materials in the irradiation path. This severely limits the usefulness of conventional imaging coils, which contain highly attenuating parts such as capacitors and preamplifiers in an unknown position, and requires development of a dedicated radiofrequency (RF) coil with close consideration of the materials and components used.

Purpose: In MR-guided radiation therapy in the human torso, imaging coils with a large FOV and homogeneous B_1 field distribution are required for reliable tissue classification. In this work, an imaging coil for MR-guided particle therapy was developed with minimal ion attenuation while maintaining flexibility in treatment.

Methods: A birdcage coil consisting of nearly radiation-transparent materials was designed and constructed for a closed-bore 1.5 T MR system. Additionally, the coil was mounted on a rotatable patient capsule for flexible positioning of the patient relative to the beam. The ion attenuation of the RF coil was investigated in theory and via measurements of the Bragg peak position. To characterize the imaging quality of the RF coil, transmit and receive field distributions were simulated and measured inside a homogeneous tissue-simulating phantom for various rotation angles of the patient capsule ranging from 0° to 345° in steps of 15°. Furthermore, simulations with a heterogeneous human voxel model were performed to better estimate the effect of real patient loading, and the RF coil was compared to the internal body coil in terms of SNR for a full rotation of the patient capsule.

Results: The RF coil (total water equivalent thickness (WET) ≈ 420 µm, WET of conductor ≈ 210 µm) can be considered to be radiation-transparent, and a measured transmit power efficiency ($B_1^+/\sqrt{P}$) between 0.17 $\mu T/\sqrt{W}$ and 0.26 $\mu T/\sqrt{W}$ could be achieved in a volume ($\Delta z = 216$ mm, complete x and y range) for the 24 investigated rotation angles of the patient capsule. Furthermore, homogeneous transmit and receive field distributions were measured and simulated in the transverse, coronal and sagittal planes in a homogeneous phantom and a human voxel model. In addition, the SNR of the radiation-transparent RF coil varied between 103 and 150, in the volume ($\Delta z = 216$ mm) of a homogeneous phantom and surpasses the SNR of the internal body coil for all rotation angles of the patient capsule.

Conclusions: A radiation-transparent RF coil was developed and built that enables flexible patient to beam positioning via full rotation capability of the RF coil and patient relative to the beam, with results providing promising potential for adaptive MR-guided particle therapy.

KEYWORDS

interventional MRI, MR-guided particle therapy, rotatable body coil

1 | INTRODUCTION

Effective cancer treatment with radiotherapy aims to maximize toxicity to the tumor while minimizing the dose to surrounding healthy tissue, especially to organs at risk. This requires imaging to optimize the treatment plan and to customize the dose distribution based on tumor size and shape, while also sparing the healthy tissue as best as possible. Reliable identification of tissue types, especially cancerous tissue, is crucial for dose calculation, so the clinical outcome is highly dependent on the quality of the imaging method chosen. Due to the superior soft-tissue contrast of MRI compared to CT, MR-guided radiotherapy (MRgRT) has recently gained more and more interest in the field and is proving to be a viable alternative to conventional CT-based radiotherapy planning.[1] In addition, the absence of ionizing radiation allows for imaging without additional dose exposure to the patient, and the risk of radiation-induced secondary cancer can be avoided,[2] thereby, enabling more accurate and, if required, more frequent monitoring of the patient's status throughout the treatment course. As a consequence, changes in tumor size, anatomical or physiological processes, and patient positioning between radiation fractions can be tracked and accounted for by interfractional modifications to the initial treatment plan. In addition, real-time imaging of the patient's movement, breathing or heartbeat is possible with fast MR sequences such as bSSFP[3] (balanced Steady State Free Precession), thus also allowing for intrafractional adjustments to the treatment during a session.[4] This flexibility in adaptive radiotherapy has the potential to considerably improve the quality of the treatment in clinical practice.[5–8]

If particle therapy is combined with MRI, the necessary accuracy of the target volume localization can be achieved and the dose exposure to surrounding healthy tissue can be further reduced due to the spatially confined energy absorption of ions in water-like tissue.[9,10] This is particularly relevant for cancers adjacent to radiation-sensitive tissue such as the brain stem, the spinal cord or internal organs, or when treating pediatric cancer, as it can increase quality of life.[11–13] Another aspect of particle therapy is the flexibility in choosing the type of ions for the irradiation. This choice offers an additional degree of freedom for treatment, since the number and energy of the secondary electrons and the corresponding relative biological effectiveness (e.g., ratio of photon to charged particle dose resulting in the same biological effect) in tissue depend on the ion species.[14] Modern facilities can accelerate different types of ions ($^1H^+$, $^4He^{2+}$, $^{12}C^{6+}$) for irradiation and adjust the treatment depending on the tumor modalities. The number of studies investigating other heavy ions with expected clinical benefit, such as $^{16}O^{8+}$ or $^{7}Li^{3+}$, is limited up to now.[15]

While the compatibility of MR guidance with radiotherapy has been demonstrated in vivo,[16] the transition from traditional photon radiotherapy to particle therapy remains an ongoing challenge. Beside the need for Monte Carlo simulations to predict the trajectories of charged particles in magnetic fields prior to beam delivery,[17] there are several constraints on the magnet system and the hardware components in use. Considering that ions are subject to inelastic Coulomb interaction, the range of charged particles strongly depends on the properties of the penetrated materials. Since the energy transfer from ions to matter is not linear along the penetration path, but increases sharply near the penetration depth (also known as the Bragg peak), even small deviations in beam delivery or tissue distribution from the planned treatment situation can severely impair the treatment success. Known uniform beam attenuation can be compensated to some extent with higher initial beam energy or a thinner attenuator. However, non-homogeneous material distributions lead to uneven beam scattering, which cannot be corrected. Consequently, discrete electronic components of an RF coil should not be located in the path of the ion beam (e.g., capacitors, preamplifiers, etc.) and a small conductor thickness with negligible ion attenuation is favorable.

In general, RF coils are required to excite the spin system and to acquire the MR signal of the excited spin ensemble during readout. Thus, RF coils serve as a connection between the object to be examined and the MR scanner. The quality of an RF coil is crucial for proper imaging and depends, among other things, on the electrical conductivity of the conductor used. Hence, there is a lower limit for the conductor thickness characterized by the depth of penetration into the conductor (skin depth) for the given RF frequency.

Furthermore, the treatment quality strongly depends on the flexibility and precision of the patient positioning. In contrast to conventional radiotherapy, in which the photon source is relatively small and can be rotated around the patient with little effort, particle therapy requires large accelerator facilities and flexibility in treatment planning is difficult to achieve. Because the ions are accelerated to relativistic energies during treatment, bending the particle beam is challenging, and requires large and expensive gantry systems[18] that are beyond the scope of many radiation centers. A rotatable patient positioning system enables beam access from various angles even for a fixed ion source, therefore eliminating the need for a costly gantry system to achieve different angles of irradiation and allowing more flexible treatment planning for many radiation centers.[19–21] This treatment flexibility facilitates better sparing of organs at risk and leads to greater precision in tumor irradiation. The rotation of the patient leads to body contour changes and organ displacements or movements, which occur due to the change in the direction of gravity at different patient positions. MR imaging is particularly suitable for detecting anatomical changes due to its high soft tissue contrast, and can be used as a basis for organ recontouring and for recalculation of the dose distribution with Monte Carlo simulations. Thus, an “on-table” adaptation and optimization of the radiation plan (e.g., different beam energy and/or raster scanning of the target volume) could be realized and implemented using deformable image registration.[22,23]

The aim of this work was the design and construction of an RF transmit and receive body coil for MR guidance that is compatible with particle therapy. For this purpose, homogeneous imaging in a large FOV with high SNR is advantageous, as covering the complete torso facilitates treatment planning of many organs and allows for a wider range of applications. Common closed-bore MR systems are not suitable for reliable beam delivery due to beam attenuation or scattering at the gradient coil, cryostat, or other components of the MR scanner. Thus, for irradiation with particle beams, an open-bore MR system[24] (e.g., double-doughnut shaped) is required in the final setup.

However, this study addresses the feasibility of MRgPT and the concept of MR imaging in combination with a patient rotation system. Therefore, the focus is on evaluating the imaging properties of a radiation-transparent body coil that can be rotated for more treatment flexibility and could be transferred to a different setup with an open-bore MR system. Accordingly, a closed MR system is considered sufficient in the context of this proof-of-concept study.

To demonstrate the functionality of the built RF coil under its full rotation, transmit and receive field distributions of the RF coil were experimentally obtained at various rotation angles in a horizontal closed-bore 1.5 T MR system and compared to simulations as well as to the internal RF body coil of the MR scanner. Since the rotation of the patient may impact the tuning of the RF coil and affect its imaging capabilities, the transmit and receive field distribution were investigated with a phantom and a human voxel model across different rotation angles. For a detailed characterization of the imaging properties of the built RF coil, the SNR was measured across different rotation angles of a phantom and compared with the SNR of the internal body coil.

2 | METHODS

2.1 | RF coil

To meet the requirement of a homogeneous RF field distribution in a large FOV sufficient for full body cross section imaging, an unshielded cylindrical 16-rung

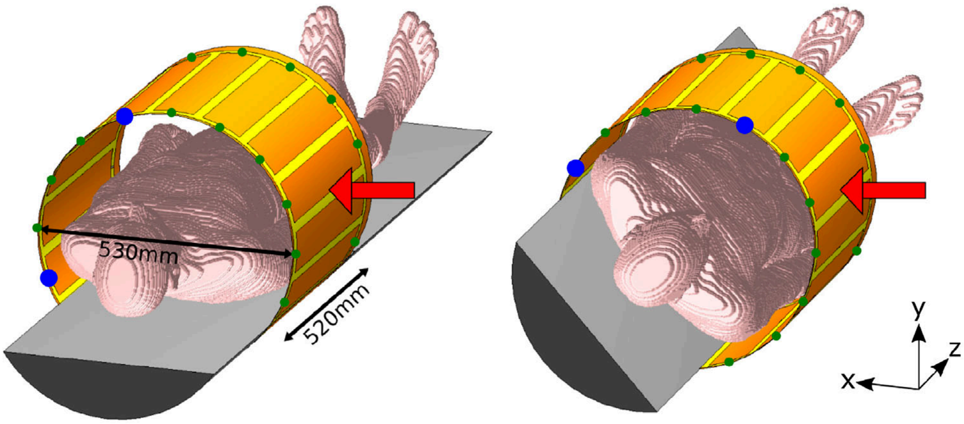

FIGURE 1 3D model of the RF coil with a voxel-based body model serving as realistic patient loading (CST voxel model: Gustav, 38 y, 176 cm, 79 kg, male) on top of a tailored pad (gray) and including tuning capacitors (green circles) and two matching networks (blue circles). The human voxel model is shown in feet-first position along the z-axis of the RF coil's coordinate system (x, y, z), which is shifted by 56 mm in y-direction with respect to the coordinate system of the MR scanner (X, Y, Z). Due to the high-pass birdcage configuration, all capacitors are located in the end rings of the RF coil, and a large window between the end rings is essentially transparent for radiation treatment. A potential ion beam is indicated by a red arrow. Patient rotation allows irradiation from multiple angles even with a static ion source.

birdcage resonator[25,26] was built for a 1.5 T MR system (Sola, Siemens Healthineers, Erlangen, Germany) with the B_0 field along the bore of the magnet.

The chosen high-pass birdcage configuration is particularly suitable, as the capacitors are located on the end rings only and, therefore, additional ion attenuation and scattering can be avoided over a large section of the RF coil in between the end rings[27] (Figure 1). As the birdcage design can operate as both a transmit and receive coil, no additional RF surface coils are required, thus further reducing interference with the ion beam.

Furthermore, the patient can be rotated together with the RF coil, which allows 360° access to the patient and the selection of optimal treatment parameters even with a fixed ion beam source. For this purpose, the patient is located inside a cylindrical capsule with a wall thickness of 1 cm and an outer diameter of 55 cm (Figure 2a). Vacuum mattresses and pillows (Figure 2c) provide the necessary stability for patient fixation during treatment. Instead of the patient table of the scanner, a dedicated wooden table with rollers supports the patient and enables positioning and rotation of the patient capsule.

This setup leads to a mismatch of the center of the patient capsule (x, y, z) and the isocenter of the magnet (X, Y, Z) and results in an elevated position for patients located in the center of the patient capsule ($y - Y = \Delta Y = 56$ mm). It should be noted that the unshielded coil presented here is therefore also not centrally aligned with the system's internal body coil and gradient coil.

The materials of the RF coil comprise a flat copper conductor (thickness = 35 µm, width = 2 cm), which is embedded between two layers of flexible polyimide and acrylic-based adhesive (Figure 2b). Due to the high dielectric strength of polyimide films of above 600 V/µm,[28] a layer of 25 µm is sufficient to achieve electrical insulation between the patient and the conductor.

In addition, the vacuum mattresses provide electrical insulation between the patient and the RF coil and act as a spacer, since a minimum distance from the electrical conductor can easily be achieved. In order to protect the capacitors on the end rings of the RF coil against mechanical stress from the vacuum mattress and to also achieve electrical insulation, dedicated protective caps were made of a photopolymer with a 3D printer and attached at the capacitor locations.

The RF coil measures 52 cm in axial (z-) direction and is split into four segments along the circumference of the cylinder due to manufacturer specifications for the flexible circuit boards. The segments are directly attached to the inner surface of the patient capsule with an additional adhesive layer and electrically connected with one another by capacitors. Consequently, the RF coil shares the inner diameter of the patient capsule of 53 cm in x- and y-direction, eliminating the need for a rigid casing and thus increasing the radiation transparency for different irradiation angles.

2.2 | Supplementary electronics

A self-built switch between RF coil and MR scanner separates the transmission (Tx) and reception (Rx) line allowing both spin excitation and signal acquisition with the RF coil (Figure 3).

In case of transmission, the receive line is blocked by diode-controlled circuits to protect the low-noise preamplifier, and the RF pulse of the MR scanner is conducted towards the RF coil. A 50 Ω termination (6550.17.AA, Huber & Suhner, Pfäffikon, Switzerland) absorbs any

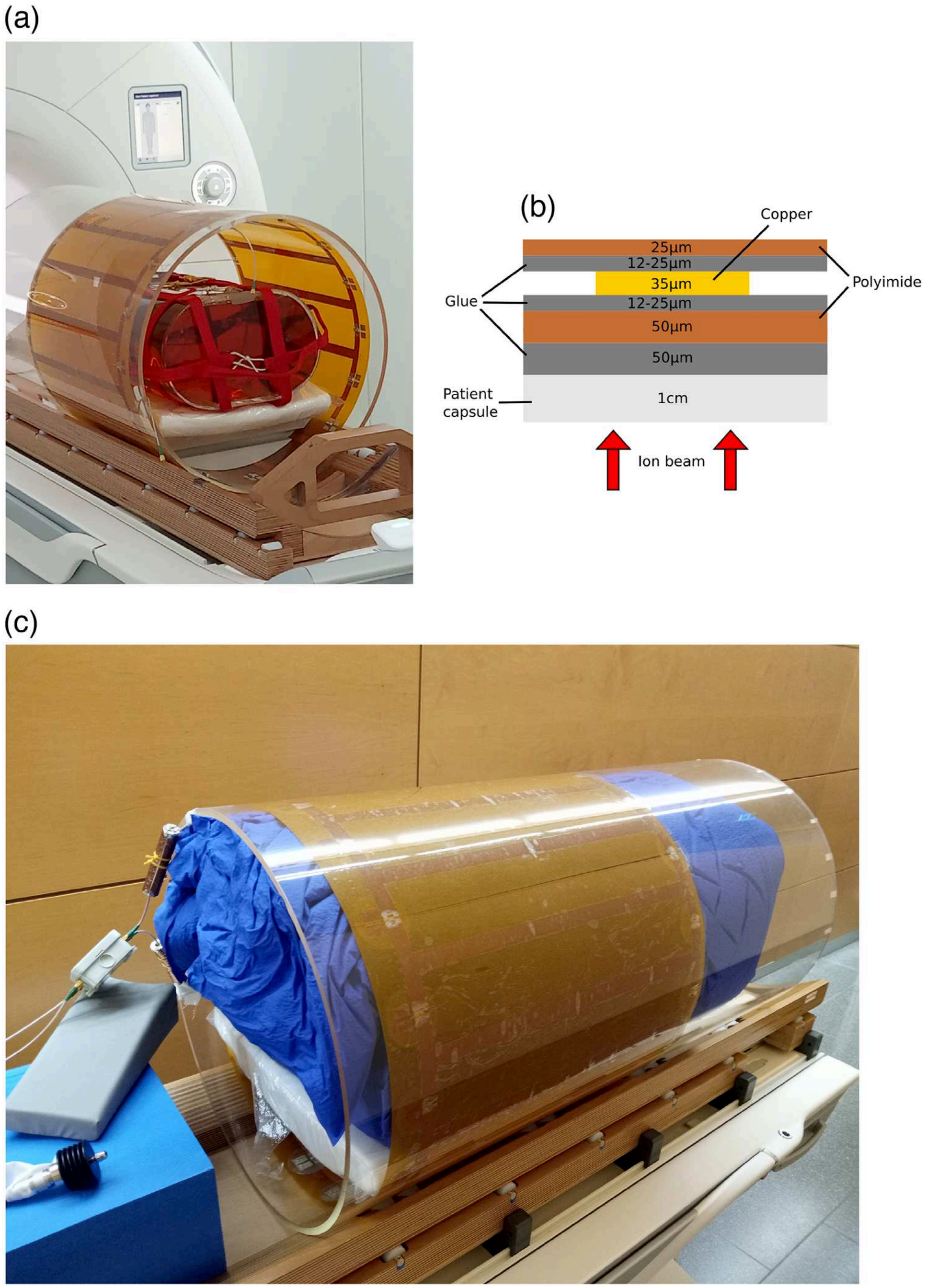

FIGURE 2 Measurement setup of the RF coil (a) attached to the patient capsule (acrylic tube) including phantom and pad. A custom-built wooden table supports the RF coil on top of the patient table of the MR imager, and integrated rollers facilitate patient rotation. The zoomed-in 2D cross section of the RF coil (b) including the patient capsule reveals the layered structure and the thickness of each material. Depending on the position of the irradiation, the ion beam (red arrow) either hits the copper conductor completely, partially or not at all. Immobilization of a phantom with vacuum mattresses is shown in subfigure (c).

power that is reflected to the output of the quadrature hybrid during transmission and dissipates it as heat. Analogously, the transmission line is blocked during receive mode. A self-built quadrature hybrid located between the RF coil and the Tx/Rx switch enables circularly polarized transmission and reception by either splitting incoming transmit RF pulses or combining MR receive signals with a 90° phase shift. Thus, the required power can be reduced during transmission and the SNR can be increased during reception.[29] RF currents on the outer conductor of the coaxial cable (K_02252_D-08, Huber & Suhner) were suppressed by inductively coupled cable traps,[30] facilitating tuning and matching of the RF coil. A reflection coefficient better than −34 dB and

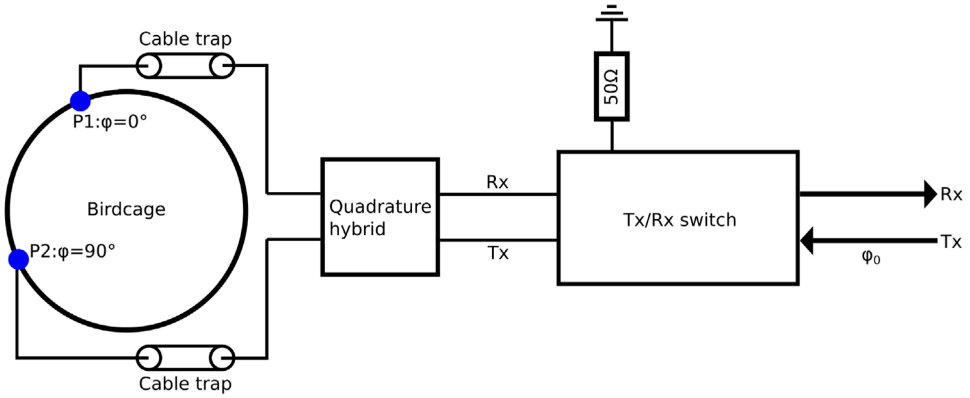

FIGURE 3 Schematics of the electrical components necessary for transmission (Tx) and reception (Rx) with the birdcage RF coil, which is driven in quadrature mode via a quadrature hybrid. RF signals at the ports P1 and P2 of the birdcage coil, which are indicated in blue, have a phase difference of $\Delta\varphi = 90°$.

a decoupling between the two ports better than −16 dB was achieved at 63.68 MHz (phantom rotated by 0°).

2.3 | Ion attenuation

In particle therapy, accelerated ions are required to travel a certain distance in water-like tissue to be suitable for effective cancer treatment. This range corresponds to an energy range of 48–221 MeV and 88–430 MeV/u for protons and $^{12}C^{6+}$ ions, respectively. For this relativistic energy range, the particle beam attenuation is dominated by the electronic stopping power of the material, while the cross section for nuclear interaction can be neglected.[31] Thus, the Bethe-Bloch equation[32] accurately describes the ion attenuation, and the stopping power primarily depends on the density of the penetrated material. For better comparison, the stopping power is usually expressed in terms of water-equivalent thickness (WET), which is given by the thickness of the penetrated material multiplied by the ratio of its stopping power and the stopping power of water. Thus, the stopping power of a penetrated material is assigned to the thickness of water that would lead to the same ion attenuation.

Accordingly, the WET for the different layers of the RF coil was calculated to estimate the effect on the particle beam. For materials composed of multiple elements, such as water or polyimide, the mass-weighted effective nuclear number was used for the calculation of the stopping power.[33] To assess the effect of the acrylic-based adhesive layers (3M467) with uncertain thickness (specified as 12–25 μm and 50 μm by db electronic GmbH, Waldshut-Tiengen, Germany) and chemical composition on the ion beam and to validate the calculations of the other materials, the stopping power was measured for the RF coil at the Heidelberg Ion Beam Therapy Center (HIT). For this measurement, the RF coil parts without the patient capsule were irradiated with $^{12}C^{6+}$ ions (FWHM = 5.1 mm, beam energy = 200.3 MeV/u) at three different positions: (1) the RF coil at a position where the ion beam penetrated all layers including the conductor ("All layers"), (2) the RF coil where only half of the ion beam penetrates the conductor ("Edge of copper"), (3) the RF coil where all layers except the conductor were hit ("No copper"). The RF coil was placed at a distance of 25 cm in front of a Peakfinder water column (PTW Freiburg GmbH, Freiburg, Germany), where the remaining range of the particles could be detected by a stepwise measurement of the current in ionizing chambers along the beam axis. The resulting profile corresponds to the delivered dose to water, and the ion attenuation for different positions on the RF coil can be determined by the shift of the Bragg peak position relative to a reference measurement without RF coil parts in front of the Peakfinder water column.

The polyimide and adhesive layers as well as the patient capsule are assumed to be homogeneously distributed. Thus, the ion attenuation is almost independent of the angle of incidence and can be compensated with higher initial ion energies. However, this does not apply for layers with a non-uniform thickness, since deviations from the desired thickness can lead to heterogeneous ion attenuation and scattering of the ion beam. Therefore, tolerances that are caused by limited precision in the manufacturing process should be examined carefully. In contrast to the thin layers of the RF coil where relative errors in the manufacturing process result in minor deviations of the WET, tolerances in the patient capsule could have a greater impact. The tolerance of the wall thickness was specified as ±1 mm (Thyssenkrupp AG, Essen, Germany). To obtain a more accurate estimate of the wall thickness of the patient capsule, the wall thickness was measured at the positions of the 16 capacitors on one side of the patient capsule. Each measurement at a capacitor position consists of 10 individual measurements to reduce the error in determining the wall thickness. The stopping power of the vacuum mattresses used is small, because the filling material (styrofoam balls) has a very low density. In addition, it can be assumed that the vacuum mattresses are filled homogeneously and that there are no major changes in the stopping power throughout the volume. Hence, the ion beam attenuation of the vacuum mattresses is neglected in this study.

2.4 | Phantom

For the MRI measurements, a large cylinder phantom with ellipsoidal cross section (dimensions: 32 cm × 20 cm × 50 cm, volume: ≈ 40 L) was placed in the center of the RF coil on top of a tailored pad (Figure 1) with a minor circle segment (width: 31 cm, height: 10 cm) made of Obomodulan 210 (OBO-Werke GmbH, Stadthagen, Germany). Vacuum mattresses and additional cushions were used to prevent sliding of the phantom, especially during measurements with the rotated patient capsule. The dielectric properties of the filling material of the vacuum mattress (styrofoam balls) or the cushions are close to those of vacuum and were therefore set equal to vacuum for the simulations in this work ($\varepsilon' = 1, \sigma = 0$ S/m). Since the phantom rotates together with the patient capsule around the axial axis, the rotation of the patient capsule can be defined with respect to the horizontal position of the phantom (0° rotation), where the major axis of the ellipsoidal cross section coincides with the horizontal x-axis of the patient capsule. The phantom housing is made of PMMA (polymethylmethacrylate), which is filled with a homogeneous liquid containing water, polyvinylpyrrolidone and sodium chloride.[34] The measured dielectric properties are similar to those of the human torso[35,36] ($\varepsilon' = 55.5, \sigma = 0.43$ S/m at 64 MHz); thus, the phantom was found suitable to imitate the load of a patient on the RF coil.

Electromagnetic field simulations were performed in CST Studio Suite 2020/21 (Dassault Systèmes, Vélizy-Villacoublay, France) at 63.9 MHz.[37] The simulated phantom was created to resemble the real phantom in dimensions as well as dielectric properties.[34] In addition, a heterogeneous human voxel model (CST voxel model: Gustav, 38 y, 176 cm, 79 kg, male) (Figure 1) with asymmetrical shape and tissue distribution was implemented to simulate a more realistic loading of the RF coil.

2.5 | Acquisition of B_1 field maps

Transmission and reception characteristics of the proposed RF coil were investigated in the phantom in simulation and measurement. The measured flip angle and receive sensitivity maps were obtained using the double-angle method.[38] Data was acquired with a slice thickness of 4 mm and a nominal spatial resolution of (4 mm^2) in slices with a FOV of 256 mm × 256 mm in sagittal, 384 mm × 256 mm in coronal and 384 mm × 240 mm transversal direction. For the patient capsule rotated by 30°, a larger FOV was acquired with 312 mm × 256 mm, 384 mm × 256 mm and 384 mm × 312 mm for sagittal, coronal and transverse slices, respectively. Since the z position of the patient rotation system and the rotation angle had to be adjusted manually, a fingertip-sized PinPoint (Beekley Medical, Bristol, USA) was placed at the top center of the phantom to verify the z position in the MR images for each rotation angle. After manual adjustment of the resonance frequency, the MR signal was obtained using a gradient-echo sequence with TE = 10 ms and TR = 10 s and pulse voltages of 160 V and 320 V and target flip angles of $\alpha_1 = 60°$ and $\alpha_2 = 120°$. From the two acquired MR images, a flip angle map for the 160 V pulse was calculated. Since the phantom is homogeneously filled, the relative sensitivity map $B_{1}{}^{-}{}_{,rel}$ could then be calculated with the relationship $S(x) \propto \sin(\alpha(x)) \cdot B_{1}{}^{-}{}_{,rel}(x)$ and normalized to its respective maximum value. Depending on the FOV, the total acquisition time amounted to 10–20 min per slice. For a quantitative evaluation of transmit field ($B_1{}^+$) and receive sensitivity ($B_1{}^-$) profiles, the transmit power efficiency and the receive field were calculated from the measured flip angle map and compared to the simulated transmit and receive fields in the central slice of the phantom in sagittal, coronal and axial direction. Reference measurements with the scanner's internal body coil were performed with the same average flip angle to compare the performance. These measurements and simulations allow a comparison between the built RF coil and the internal RF coil inside the MR scanner.

To further characterize the performance of the built RF coil under rotation of the patient capsule, 2 · 24 additional simulations (2 cases: phantom with elevated position with respect to the isocenter of the magnet (y = Y + 56 mm) and a human voxel model excluding the arms (y = Y + 56 mm)) and 2 · 24 additional measurements (2 cases: 2 pulse voltages 170 V, 340 V) with a voxel size of (6 mm)^3 were performed to cover a full rotation of the patient capsule in increments of 15°. Each rotation angle was verified with a localizer and thereafter the gradient-echo sequence from above was used to acquire 3D data with a FOV of 384 mm × 384 mm in x- and y-direction and 42 slices in z-direction in less than 11 min per pulse sequence. The GRE sequence parameters were adjusted to TE = 5 ms, TR = 10 s and target flip angles of $\alpha_1 = 60°$ and $\alpha_2 = 120°$. Similar to above, the 3D $B_1{}^+$ and $B_1{}^-$ field distributions were calculated from the two MR images. As quantitative analysis of the simulated and measured B_1 field distributions of the developed RF body coil, the mean of the transmit power efficiency ($B_1^+/\sqrt{P}$) and the relative receive sensitivity profile ($B_1{}^-{}_{,rel}$) was determined in the entire phantom volume within a range of $\Delta z = 216$ mm in the center of the phantom (-108 mm $\leq z \leq +108$ mm) for all rotation angles of the patient capsule. In order to also evaluate the simulated and measured RF field homogeneity inside the phantom and the human voxel model, the standard deviation was calculated in the same volume. For this purpose, a minimum signal intensity of the individual images was defined as threshold in order to determine the voxels within the phantom volume and to obtain a mask for the mean calculation. Partial volume effects at the edge of the phantom were removed by slightly reducing the size of the mask.

The SNR of the built RF coil was determined in the center of the phantom within the volume of $\Delta z = 216$ mm using a threshold to determine the signal intensity of the images with a flip angle of 60° at the 24 different rotation angles of the patient capsule. Correspondingly, an additional maximum signal intensity was defined as a threshold in order to obtain a mask for the noise calculation[39] (NEMA, method 4). For an SNR comparison between the built RF coil and the internal body coil, 24 additional phantom measurements were carried out with the internal body coil using the same sequence parameters except a different pulse voltage of 185.2 V to obtain the same flip angle. The thresholds of the signal intensity in the images of the internal body coil were adjusted for each volume such that the masks for the signal and noise calculations contain the same number of voxels for both coils at a rotation angle of 0°.

3 | RESULTS

3.1 | Ion attenuation

The calculated stopping powers (Figure 4a, b) for the layers of the proposed RF coil show a dominant ion attenuation of the conductor for the given energy range, corresponding to 2.6–7.7 MeV/mm for protons and 65.9–174.4 MeV/mm for carbon ions. However, the energy dependence of the stopping power is similar for the different materials and the stopping power ratio of the materials with respect to water can be considered constant (Figure 4c, d) for the given energy range.

The average stopping power ratio for protons and carbon ions corresponds to ≈ 6.70 ($^1H^+$) / ≈ 6.79 ($^{12}C^{6+}$) for copper, ≈ 1.43 for polyimide and ≈ 1.21 for PMMA. For a 35 µm thick conductor of pure copper, this results in a calculated average WET of ≈ 235 µm for protons and ≈ 238 µm for carbon ions. The measurements with the Peak finder reveal a sharp Bragg peak (Figure 5) of the dose distribution along the beam axis.

Subtracting the change in peak position relative to a reference measurement of the target with and without the copper layer (Table 1), the WET of the conductor amounts to ≈ 210 µm (subtraction: 420 µm–210 µm), which is close to the calculated value of 236 µm with a stopping power ratio of ≈ 6.74 ($^{12}C^{6+}$) at 200.3 MeV/u.

TABLE 1 Shift of the Bragg peak position relative to a reference measurement using $^{12}C^{6+}$ ions that penetrated different layers of the radiation-transparent RF coil.

Target	Change in peak position [mm]	80% peak width [mm]	90% peak width [mm]
All layers	0.42	0.90	0.56
Edge of copper	0.34	0.93	0.59
No copper	0.21	0.91	0.57
Reference: No target	0.00	0.90	0.58

Note: The value for each layer composition was averaged for two different positions on the radiation-transparent RF coil. The peak width was determined at 80% and 90% of the measured maximum ionization current in the Peakfinder.

The ion attenuation of the adhesive layer and the polyimide layer can be compensated with higher beam energies as they are homogeneously distributed along the radiation-transparent RF coil. Additionally, the width of the Bragg peak was examined at 80% and at 90% of the maximum value, and no substantial broadening of the peak width along the beam axis was observed for the different targets. Therefore, beam scattering along the beam axis is considered negligible even if the ion beam hits the edge of the conductor.

The mean of all averaged wall thicknesses of the patient capsule corresponded to 9.291 mm, with a standard deviation of 0.073 mm. The largest deviation in averaged wall thicknesses between two adjacent capacitors comprised 103 µm, leading to a difference of ≈ 120 µm for the WET. Additional measurements in between the capacitors suggest that the wall thickness between capacitors changes gradually and can be considered rather uniform. Consequently, the ion attenuation of the patient capsule plays a minor role compared to the copper layer.

3.2 | Phantom measurements

For the MR measurements, the transmit power efficiencies of the proposed radiation-transparent RF coil were determined for the three central planes inside the homogeneous phantom with horizontal position (0° rotation) and compared to simulations and the internal body coil of the MR system (Figure 6).

The presented transmit RF field patterns illustrate the resemblance in the characteristics of the radiation-transparent coil, its simulation and the internal coil. The RF field distributions show slight inhomogeneities especially towards the edges of the homogeneous phantom in the transverse (Z = 0 mm) and the sagittal (X = 0 mm) plane; however, similar asymmetries have already been reported in literature for the given frequency.[40,41] In the

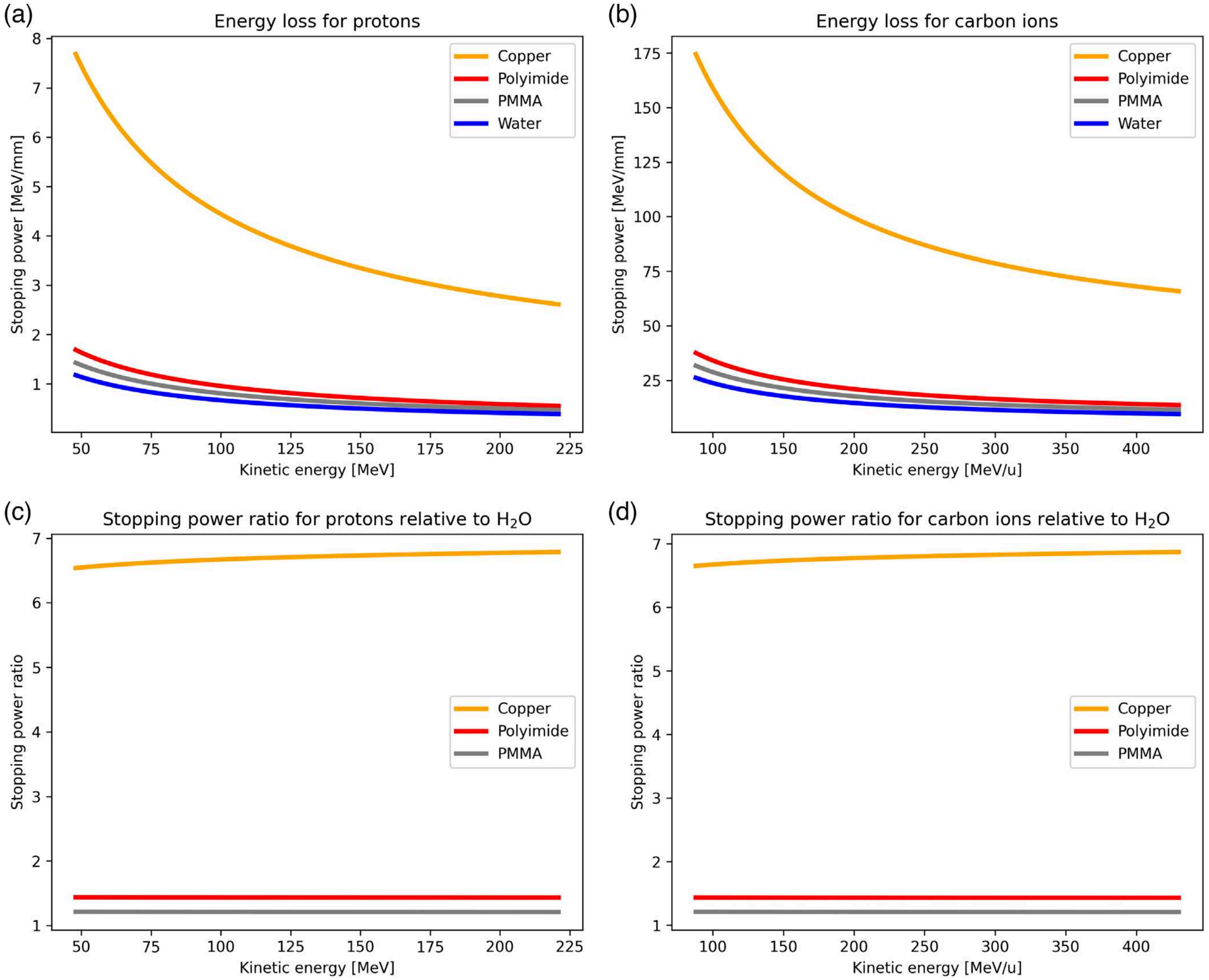

FIGURE 4 Calculated stopping power of the materials used in the radiation-transparent RF coil for the given energy range of $^{1}H^{+}$ (a) and $^{12}C^{6+}$ ions (b). The ratio of the stopping power of the material relative to water is shown for the relevant energy range of $^{1}H^{+}$ (c) and $^{12}C^{6+}$ ions (d).

coronal slice (Y = 56 mm), the measured B_1^+ field distribution of the radiation-transparent RF body coil appears to be more uniform compared to the simulated field pattern in the homogeneous phantom. While the measured transmit power efficiency of the radiation-transparent RF body coil remains below the simulated one for all slices, it exceeds the transmit power efficiency of the internal body coil. Heterogeneous structures in the human voxel model lead to a decreased homogeneity of the RF field distribution. Similar results for the transmit power efficiency could be achieved for a phantom and voxel model rotated by 30° with respect to the z-axis of the MR scanner (Figure S1), indicating little impact of the RF coil rotation on the transmit field.

For a more detailed analysis of the transmit field in a larger region of interest and to investigate the effect of coil rotation on the transmit field, the mean transmit power efficiency in a volume (Δz = 216 mm) at the center of the homogeneous phantom and the heterogeneous voxel model was calculated for a complete rotation of the patient capsule (0°–345°) in steps of 15° (Figure 7).

The average transmit power efficiencies correspond to 0.17–0.26 $\mu T/\sqrt{W}$ for the phantom measurements, 0.30 $\mu T/\sqrt{W}$ for the phantom simulation, and 0.27–0.31 $\mu T/\sqrt{W}$ for the human voxel model, depending on the rotation angle of the patient capsule. The standard deviation of the measured transmit power in the phantom volume varies between 0.01 and 0.02 $\mu T/\sqrt{W}$ for all rotation angles, indicating a homogeneous transmit field distribution over a large FOV.

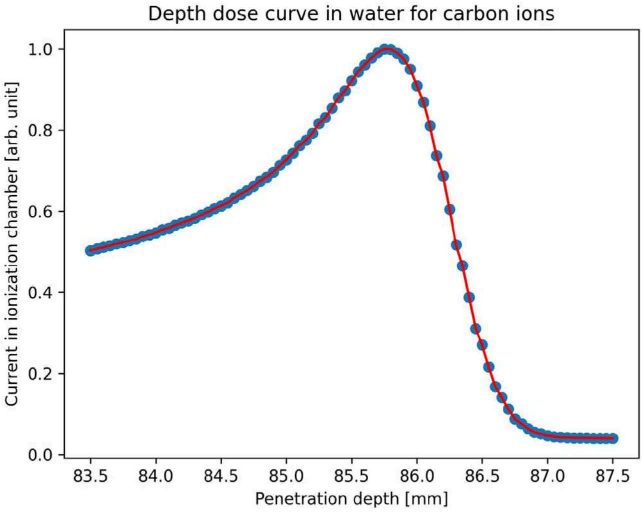

FIGURE 5 Measurement of the Bragg peak position using the Peakfinder water column to assess the range of the ions in water-like tissue after penetrating all layers of the radiation-transparent RF coil including the conductor. The ionization current in the ionization chamber is indicated in blue for each position with a step size of 0.05 mm.

Compared to the simulations, the measurements show a slight dependence on the rotation angle, with increased transmit power efficiencies at rotation angles close to 0° and 180°. The transmit power efficiency of the human voxel model appears to be slightly increased for multiples of 45° of the rotation angle.

To further evaluate the imaging performance of the radiation-transparent RF body coil, the relative receive sensitivity profiles of the RF coil were determined for the three central planes inside the homogeneous phantom with horizontal position (0° rotation) and compared to simulations and the internal body coil of the MR system (Figure 8).

The relative receive sensitivity profiles ($B_{1}{}^{-}{}_{,rel}$) indicate uniform signal acquisition of the radiation-transparent RF body coil in all three central slices. In addition, the RF field patterns show good agreement between measurement and simulation. Inhomogeneities in the receive sensitivity profiles appear to be mirrored compared to the transmit field distributions (Figure 6).

Analogous to the transmit power efficiency, a high similarity between the relative receive sensitivity profiles with a phantom or voxel model were obtained in simulation and measurement in horizontal position as well as when rotated by 30° with respect to the z-axis of the MR scanner (Figure S2).

To further evaluate the effect of rotation of the patient capsule on the receive field, the average measured and simulated receive sensitivity in a volume ($\Delta z = 216$ mm) was determined for a complete rotation of the phantom and voxel model and normalized relative to the average receive sensitivity at the horizontal position (0° rotation) (Figure 9).

Compared to the horizontal position (0° rotation), the measured relative receive sensitivity decreases for rotation angles between 15° and 120° as well as for 205° and varies between 62% and 125%. While the simulated receive field sensitivity in the homogeneous phantom is almost constant for all rotation angles, a slightly reduced sensitivity compared to the horizontal position can be observed for the human voxel for all rotation angles except for multiples of 45°. The measured standard deviation of the mean relative receive sensitivity for different rotation angles corresponds to 8%–15% in the phantom volume ($\Delta z = 216$ mm), indicating a homogeneous receive sensitivity profile in a large FOV.

A detailed examination of the transmit and receive RF field distributions in terms of homogeneity for different rotation angles was performed for the phantom measurement ($y = Y + 56$ mm), the phantom simulation ($y = Y + 56$ mm), the human voxel model ($y = Y + 56$ mm), and a phantom simulation with a hypothetical position at the isocenter of the magnet ($y = Y$) (Figure S3). The coefficient of variation (COV = standard deviation / mean) for a ROI in the transverse, coronal, and sagittal slices shows that the off-axis rotation of the elevated patient capsule contributes to the angular dependence of the RF field homogeneity (Figure S3 B, C).

A direct examination of the transmit and receive field distributions for a complete rotation of the radiation-transparent RF body coil in steps of 15° confirms the similarity of simulation and measurement, which indicates good modeling knowledge of the system (Animation S1). In addition, the simulation with the human voxel model also suggests rather homogeneous transmit and receive profiles in the torso, despite some inhomogeneities in the arms near the RF coil.

The SNR comparison between the radiation-transparent RF coil and the internal body coil shows the dependence of the SNR on the rotation angle of the patient capsule (Figure 10): A slight dependence on the rotation angle of the patient capsule can be observed for the radiation-transparent RF body coil. However, the SNR of the radiation-transparent RF coil surpasses the SNR of the internal coil at all rotation angles.

4 | DISCUSSION

This work focuses on the challenging task to unite MRI and radiotherapy with particles. The radiation-transparent RF coil presented here exhibits homogeneous imaging capability in a large FOV and thus fulfills essential requirements for meaningful imaging of tissues in whole-body measurements. For clinical application with the aim of adaptive radiotherapy in terms of patient positioning and tumor tracking or real-time gating, it is advantageous to combine MRI and radiotherapy in a single unit such as the MR-Linac.[4] The

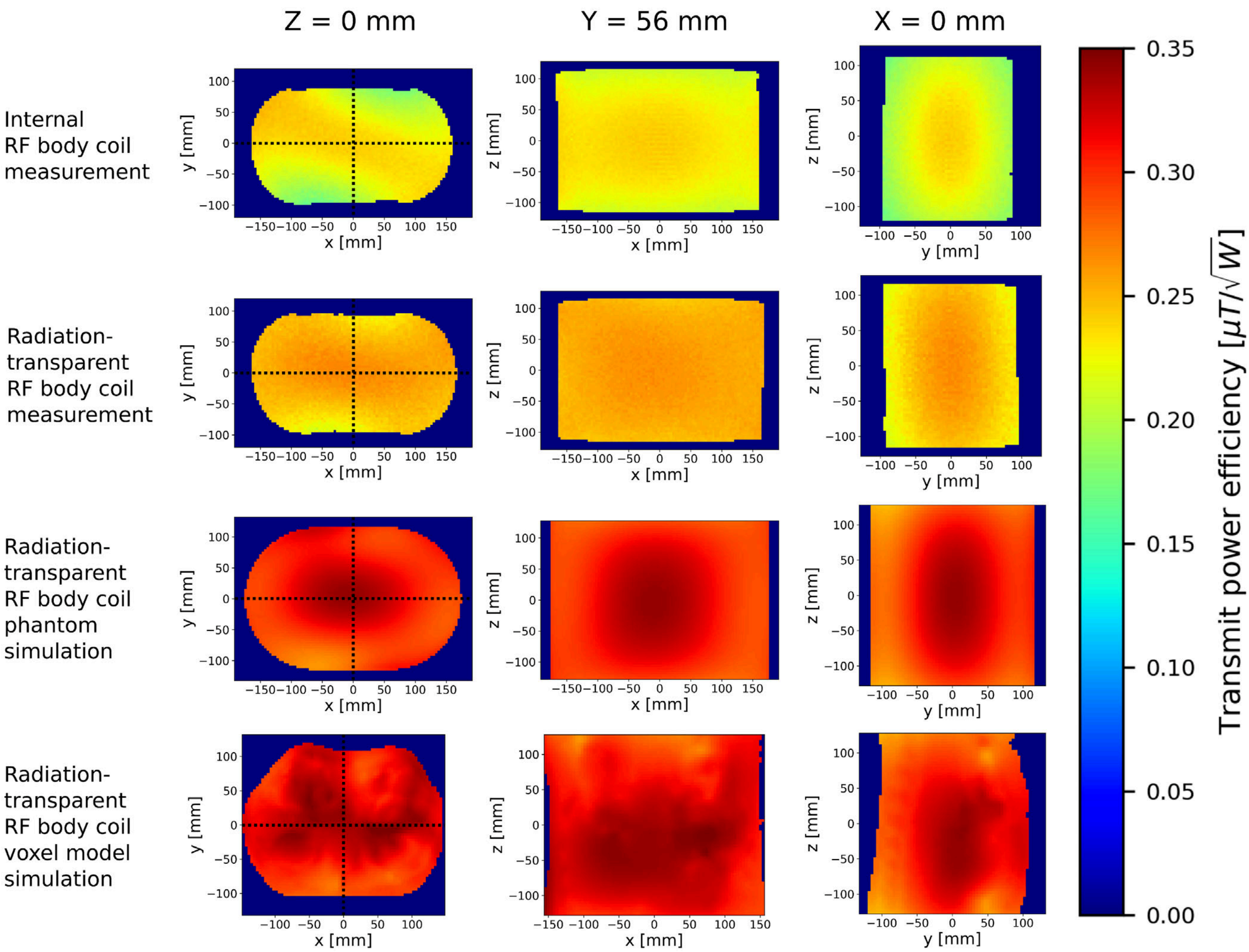

FIGURE 6 Measured and simulated transmit power efficiency of the radiation-transparent RF body coil shown in the three central slices inside a homogeneous phantom and a heterogeneous human voxel model in horizontal position (0° rotation) as well as the measured transmit power efficiency of the internal body coil. The X-, Y-, and Z-coordinates mark the position of the 2D slices (indicated in black) with respect to the isocenter of the magnet, while x, y and z denote the coordinates of the patient rotating system. To exclude extreme values at the edge of the phantom caused by the double angle method, the margin of the phantom was removed from the measured B_1 field distribution. The measured and simulated 2D data was acquired with a voxel size of $(4\text{ mm})^3$.

most common hardware in this configuration is the combination of a large body coil for transmission and a local surface coil, leading to high SNR because of the proximity to the patient. Often the local receiving coil is located within the irradiation window and leads to additional beam attenuation, which might have a negative impact on the treatment quality. While this effect can be of minor importance in conventional radiotherapy with photons,[42] particle therapy is more susceptible to non-homogeneous materials in the irradiation path.[14] Consequently, the presented design of an effectively radiation-transparent Tx/Rx body coil is preferable in particle therapy, since all attenuating materials in the irradiation window are limited to homogeneous material distributions or materials with negligible WET.

Based on the stopping power, copper has a considerably larger effect on the ion attenuation compared to the polyimide and adhesive layers as well as compared to the material of the patient capsule. A small conductor thickness is therefore favorable for the construction of an RF coil for MR-guided particle therapy. However, the minimal thickness of the conductor of the RF coil should be chosen several times thicker than the skin depth to avoid SNR losses due to suboptimal current distribution along the cross section of the conductor.[43] At 64 MHz, the skin depth amounts to 8.2 μm in copper, thus a conductor thickness of 35 μm ($\approx 4.3 \cdot$ skin depth) was chosen which corresponds to a calculated average WET of $\approx$ 235 μm for protons and $\approx$ 238 μm for carbon ions for the clinical energy range.

Considering that all capacitors are located at the end rings due to the high-pass configuration of the birdcage, patient access for the ion beam is possible from all angles. This feature enables combination with a

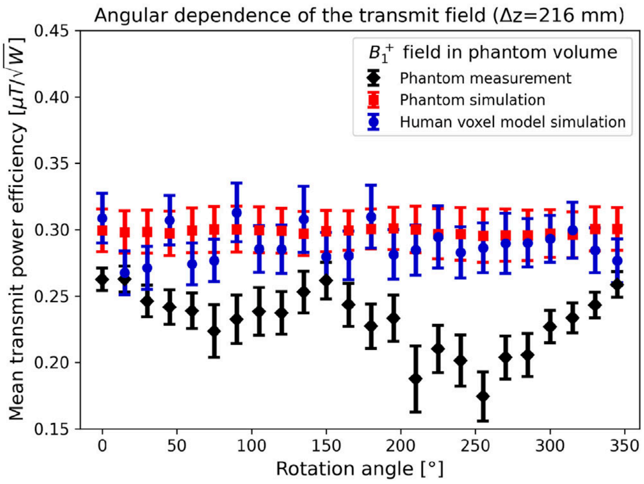

FIGURE 7 Mean transmit power efficiencies within a volume ($\Delta z = 216$ mm, complete x and y range) for different rotation angles of the patient capsule including the phantom in steps of 15°, calculated from the measurements (black) and simulations (red) in a homogeneous phantom as well as in a heterogeneous human voxel model (blue). The error bars represent the standard deviation of the transmit power efficiency in the selected volume of the phantom or voxel model for each rotation angle. The measured and simulated 3D data was acquired with a voxel size of (6 mm)^3.

rotatable patient capsule, which in turn ensures that flexible, more precise radiation treatment can be realized for a fixed ion source with no need for a costly ion gantry. In terms of imaging quality, the radiation-transparent RF body coil shows good homogeneity of the B_1 field distributions in a large FOV and high transmit power efficiency. These results were achieved in simulation and measurement and were additionally validated for different rotation angles to demonstrate the feasibility of the patient rotation system.

The compatibility of a rotatable patient positioning system with MRI has already been established for clinical field strengths using the internal body coil of the scanner.[19–21] Furthermore, the feasibility of the concept was demonstrated in a double-doughnut shaped MR-Linac with open access to the patient, thus pushing the scope one step further towards clinical radiotherapy.[21] However, these studies focused primarily on the application in MRgRT in combination with conventional photon therapy, whereas particle therapy requires a more sophisticated consideration of the beam attenuation. Conventional surface coils are non-uniform in shape and therefore result in different water-equivalent path lengths at different irradiation positions. Dense materials inside RF coils can cause additional beam attenuation and uncertainty in particle range, thus further limiting the number of RF coils compatible with particle therapy. The detailed examination of particle attenuation at clinical treatment energies for protons and carbon ions reveals a possibility for thin, homogeneous resonators for imaging. While other radiation-transparent Tx/Rx coils with an open aperture for beam access[44] also meet the requirements for particle irradiation at dedicated beam positions, the presented radiation-transparent RF body coil offers a more flexible treatment by patient rotation and excels in terms of uniformity of the B_1 field distributions. Furthermore, the setup can be easily transferred to a double-doughnut shaped MR scanner to provide access to the patient.

For the phantom measurements, a transmit power efficiency of approximately 60%–90% of the simulated transmit power efficiency in the phantom volume could be achieved for the different rotation angles of the patient capsule (Figure 7), indicating good agreement between measurement and simulation. In addition, the absolute values for the transmit power efficiency of the radiation-transparent RF body coil exceed those of the internal body coil for the three central slices of the phantom (Figure 6 and Figure S1) therefore allowing fast excitation of the nuclear spins is possible with moderate transmit powers.

The measured average receive sensitivity in the phantom volume for different rotation angles relative to the horizontal position of the phantom (Figure 9) shows a rather constant receive sensitivity of the radiation-transparent RF body coil despite a slightly increased variation under coil rotation compared to the simulations.

In terms of RF field homogeneity, the coefficient of variation (COV = standard deviation / mean) of the B_1 field distributions in the phantom volume ($\Delta z = 216$ mm) for the different rotation angles correspond to approximately 3%–14%, indicating adequate RF field homogeneity in the entire phantom.

In the simulations with the heterogeneous human voxel model, high transmit power efficiency and receive sensitivity was achieved for all rotation angles, although the B_1 field values tend to be lower than in the simulations with the homogeneous phantom. This is most likely associated with the asymmetrical shape and uneven distribution of different tissues in the voxel model. In addition, multiples of 45° of the rotation angle lead to particularly high B_1 field values. This could be related to the fact that the capacitors are located at the same position relative to the scanner if the 16-rung birdcage is rotated by multiples of 22.5° (360° / 16 = 22.5°) (Figure 1).

Despite overall good performance of the radiation-transparent RF coil, a slight deterioration in the homogeneity of transmit and receive characteristics could be observed in the measurements with a rotated phantom (Figure S3 A). For rotation angles near 0° and 180° of the patient capsule, the RF field homogeneity inside the phantom is increased, which could be explained by the symmetrical shape of the phantom and the tuning and matching of the radiation-transparent RF coil, that was performed only at 0° rotation of the patient capsule. The angular dependence of the tuning and matching of the radiation-transparent RF coil may be related to coupling between the radiation-transparent RF coil and the

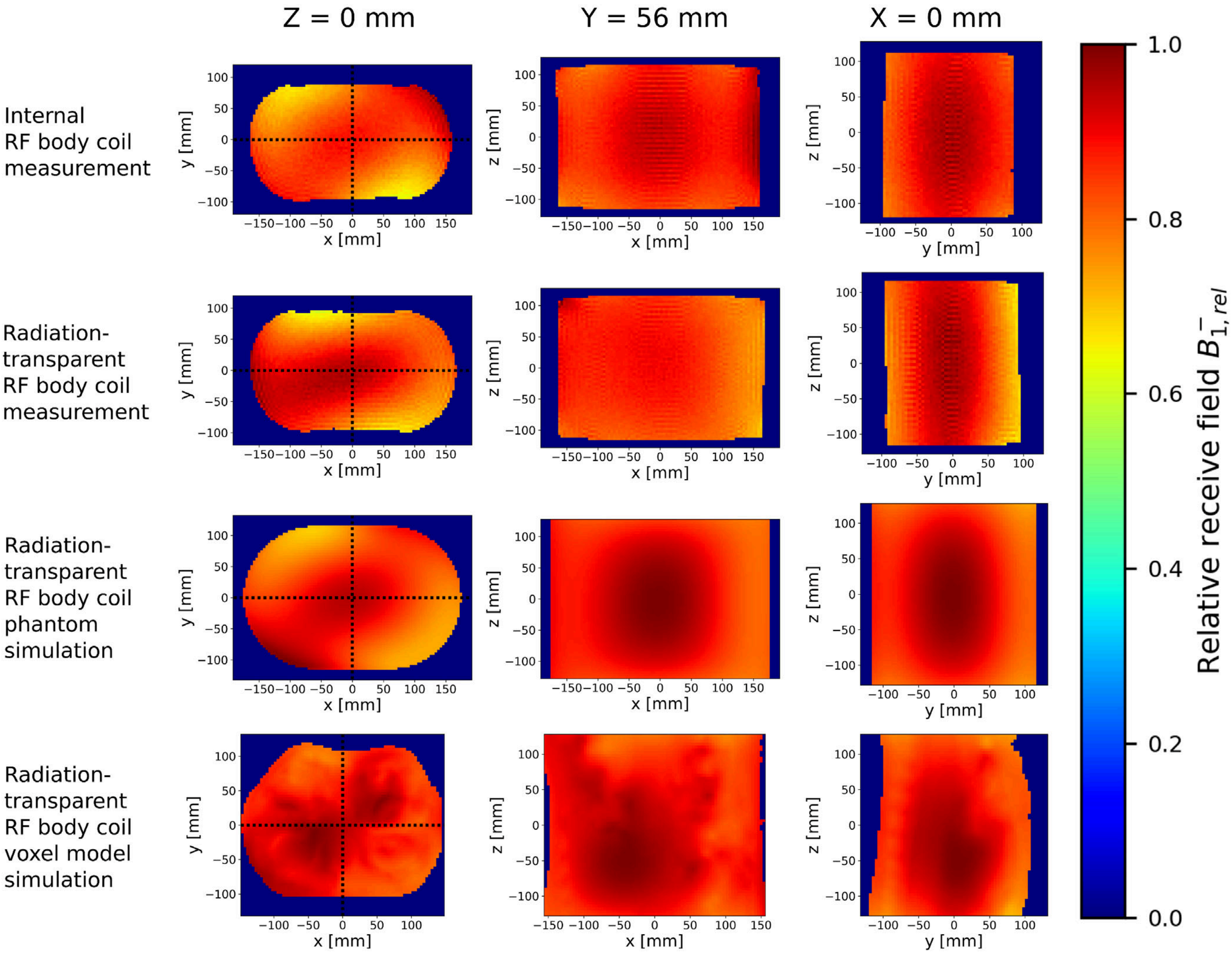

FIGURE 8 Measured and simulated relative receive sensitivity profiles of the radiation-transparent RF body coil shown in the three central slices inside a homogeneous phantom and a heterogeneous human voxel model in horizontal position (0° rotation) as well as the measured relative receive sensitivity profile of the internal body coil. The X-, Y-, and Z-coordinates mark the position of the 2D slices (indicated in black) with respect to the isocenter of the magnet, while x, y, and z denote the coordinates of the patient rotating system. To exclude extreme values at the edge of the phantom caused by the double angle method, the margin of the phantom was removed from the measured B_1 field distribution. The measured and simulated 2D data was acquired with a voxel size of $(4\ \text{mm})^3$.

internal RF coil or gradient coil of the MR scanner. The simulated results (Figure S3 B) do not show this behavior to the same extent, which may be linked to the unknown and therefore estimated diameter and setup of the internal RF coil and gradient coil in the 3D model of the MR scanner used for simulation. However, the simulated results (Figure S3 B, C) suggest a substantial reduction of the dependence of the homogeneity of the B_1 field distributions on the rotation angle if the rotation axis of the radiation-transparent RF coil including the phantom coincides with the isocenter of the MR scanner (y = Y).

In terms of imaging quality, the radiation-transparent RF body coil achieved an SNR between 103 and 150 across different rotation angles of the patient capsule in a subvolume of Δz = 216 mm (Figure 10), which corresponds to an increase in the SNR of the internal body coil by 10%–43%. Compared to the internal body coil, the RF coil presented here offers a higher SNR as well as the possibility of MR-guided radiation therapy in particle therapy due to its radiation transparency. If the achieved SNR of the developed RF body coil proves to be insufficient in clinical trials where reliable tissue classification in a reasonable time is required, a radiation-transparent receive-only coil closer to the patient and with a higher SNR could be developed.

A restriction of the proposed configuration is the predefined longitudinal axis of the patient parallel to B_0, which results in limited patient access beyond lateral irradiation in a double-doughnut shaped MR scanner and thereby reduces treatment flexibility. In this study, simulations and measurements were performed

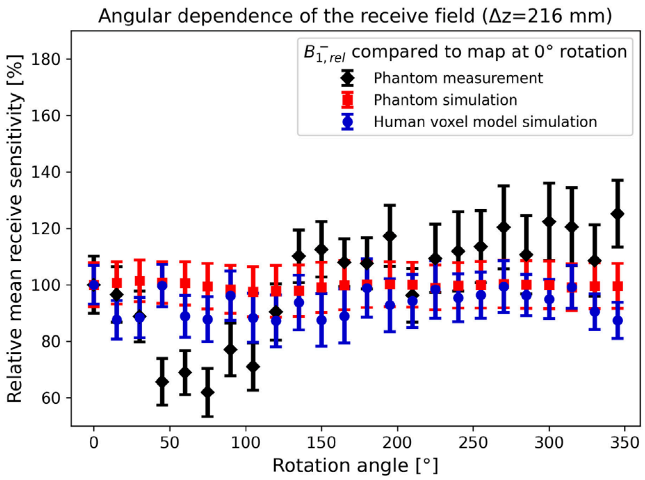

FIGURE 9 Receive sensitivity within a volume (Δz = 216 mm, complete x and y range) for different rotation angles of the patient capsule in steps of 15° relative to the corresponding receive sensitivity in horizontal position (0° rotation), calculated from the measurements (black) and simulations (red) in a homogeneous phantom as well as in a heterogeneous human voxel model (blue). The error bars represent the standard deviation of the relative receive sensitivity in the selected volume of the phantom or voxel model for each rotation angle. The measured and simulated 3D data was acquired with a voxel size of $(6\ \text{mm})^3$.

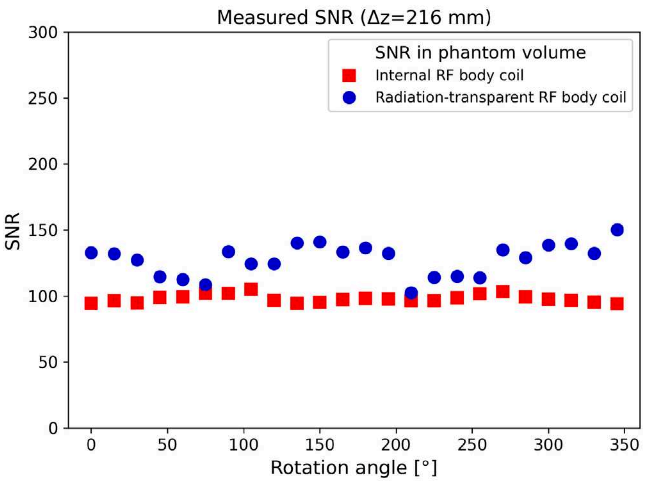

FIGURE 10 Measured SNR for each rotation angle of the phantom with a comparison between the radiation-transparent coil and the internal body coil at a flip angle of 60°. The SNR was evaluated in the entire FOV of 384 mm × 384 mm along the x- and y-axes within a centered subvolume with a range of Δz = 216 mm. The thresholds used to define the signal and noise masks have been adjusted so that the number of voxels is the same for both coils. Partial volume effects could be avoided by removing the margin of the phantom for the SNR calculation.

with a homogeneous phantom and simulations with a heterogeneous human voxel model, but no actual measurements were performed in a human subject.

In future, additional measurements will be performed to confirm the performance of the radiation-transparent RF body coil also in vivo. Future studies should also investigate the short and long-term effects of irradiation with particles and verify the durability of the radiation-transparent RF coil and the influence on the quality of real-time imaging, since radiation-induced currents have been reported for photon irradiation of RF coils in MRI.[45,46]

Investigation of the patient comfort and tolerance of the patient rotation system is beyond the scope of this work, but will be addressed in a separate study where questionnaires were evaluated to assess patient acceptability in terms of anxiety, claustrophobia and motion sickness.[47–49] This includes additional tests with the patient rotation system to ensure that the patient can be quickly rescued if a measurement is aborted due to patient complaints.

5 | CONCLUSIONS

The presented RF body coil demonstrates the feasibility of MR guidance in combination with particle therapy and shows a possible realization of a particle beam-transparent birdcage design for a closed-bore 1.5 T MR system. The constructed Tx/Rx resonator does not require any additional coils (e.g., receive coil array) and could be implemented in a double-doughnut system to enable essentially attenuation-independent particle therapy. Rotation of the patient and the radiation-transparent RF body coil in a capsule provides advantageous flexibility in particle therapy and offers a simple and affordable alternative to a complex and elaborate ion gantry. The homogeneity of the B_1 field distributions in a large FOV, the transmit power efficiency, the receive sensitivity, and the SNR indicate reasonable imaging quality for thoracic, abdominal and pelvic MRI.

ACKNOWLEDGMENTS

This work received financial support from the German Federal Ministry of Education and Research within the program “Bildgeführte Diagnostik und Therapie—Neue Wege in der Intervention” under grant 13GW0436 (ARTEMIS). For the publication fee we acknowledge financial support through project DEAL.

Open access funding enabled and organized by Projekt DEAL.

CONFLICT OF INTEREST STATEMENT

The authors have no relevant conflicts of interest to disclose.

REFERENCES

1. Pollard JM, Wen Z, Sadagopan R, Wang J, Ibbott GS. The future of image-guided radiotherapy will be MR guided. *Br J Radiol*. 2017;90(1073):20160667. doi:10.1259/bjr.20160667
2. Dzierma Y, Mikulla K, Richter P, et al. Imaging dose and secondary cancer risk in image-guided radiotherapy of pediatric patients. *Radiat Oncol*. 2018;13(1):168. doi:10.1186/s13014-018-1109-8

3. Gao Y, Zhou Z, Han F, et al. Accelerated 3D bSSFP imaging for treatment planning on an MRI-guided radiotherapy system. *Med Phys*. 2018;45(6):2595-2602. doi:10.1002/mp.12924
4. Klüter S. Technical design and concept of a 0.35 T MR-Linac. *Clin Transl Radiat Oncol*. 2019;18:98-101. doi:10.1016/j.ctro.2019.04.007
5. Corradini S, Alongi F, Andratschke N, et al. MR-guidance in clinical reality: current treatment challenges and future perspectives. *Radiat Oncol*. 2019;14(1):92. doi:10.1186/s13014-019-1308-y
6. Kurz C, Buizza G, Landry G, et al. Medical physics challenges in clinical MR-guided radiotherapy. *Radiat Oncol*. 2020;15(1):93. doi:10.1186/s13014-020-01524-4
7. Spindeldreier CK, Klüter S, Hoegen P, et al. MR-guided radiotherapy of moving targets. *Radiol*. 2021;61(1):39-48. doi:10.1007/s00117-020-00781-4
8. Otazo R, Lambin P, Pignol JP, et al. MRI-guided radiation therapy: an emerging paradigm in adaptive radiation oncology. *Radiology*. 2021;298(2):248-260. doi:10.1148/radiol.2020202747
9. Hoffmann A, Oborn B, Moteabbed M, et al. MR-guided proton therapy: a review and a preview. *Radiat Oncol*. 2020;15(1):129. doi:10.1186/s13014-020-01571-x
10. Harrabi SB, Bougatf N, Mohr A, et al. Dosimetric advantages of proton therapy over conventional radiotherapy with photons in young patients and adults with low-grade glioma. *Strahlenther Onkol*. 2016;192(11):759-769. doi:10.1007/s00066-016-1005-9
11. Leeman JE, Romesser PB, Zhou Y, et al. Proton therapy for head and neck cancer: expanding the therapeutic window. *Lancet Oncol*. 2017;18(5):e254-e265. doi:10.1016/S1470-2045(17)30179-1
12. Hess CB, Thompson HM, Benedict SH, et al. Exposure risks among children undergoing radiation therapy: considerations in the era of image guided radiation therapy. *Int J Radiat Oncol*. 2016;94(5):978-992. doi:10.1016/j.ijrobp.2015.12.372
13. Mitin T, Zietman AL. Promise and pitfalls of heavy-particle therapy. *J Clin Oncol*. 2014;32(26):2855-2863. doi:10.1200/JCO.2014.55.1945
14. Jäkel O. Medical physics aspects of particle therapy. *Radiat Prot Dosimetry*. 2009;137(1-2):156-166. doi:10.1093/rpd/ncp192
15. Tommasino F, Scifoni E, Durante M. New ions for therapy. *Int J Part Ther*. 2016;2(3):428-438. doi:10.14338/IJPT-15-00027.1
16. Raaymakers BW, Jürgenliemk-Schulz IM, Bol GH, et al. First patients treated with a 1.5 T MRI-Linac: clinical proof of concept of a high-precision, high-field MRI guided radiotherapy treatment. *Phys Med Biol*. 2017;62(23):L41. doi:10.1088/1361-6560/aa9517
17. Oborn BM, Dowdell S, Metcalfe PE, Crozier S, Mohan R, Keall PJ. Proton beam deflection in MRI fields: implications for MRI-guided proton therapy. *Med Phys*. 2015;42(5):2113-2124. doi:10.1118/1.4916661
18. Haberer T, Debus J, Eickhoff H, Jäkel O, Schulz-Ertner D, Weber U. The heidelberg ion therapy center. *Radiother Oncol*. 2004;73:S186-S190. doi:10.1016/S0167-8140(04)80046-X
19. Whelan B, Liney GP, Dowling JA, et al. An MRI-compatible patient rotation system — design, construction, and first organ deformation results. *Med Phys*. 2017;44(2):581-588. doi:10.1002/mp.12065
20. Buckley JG, Rai R, Liney GP, et al. Anatomical deformation due to horizontal rotation: towards gantry-free radiation therapy. *Phys Med Biol*. 2019;64(17):175014. doi:10.1088/1361-6560/ab324c
21. Buckley JG, Dong B, Liney GP. Imaging performance of a high-field in-line magnetic resonance imaging linear accelerator with a patient rotation system for fixed-gantry radiotherapy. *Phys Imaging Radiat Oncol*. 2020;16:130-133. doi:10.1016/j.phro.2020.11.001
22. Bohoudi O, Bruynzeel AME, Senan S, et al. Fast and robust online adaptive planning in stereotactic MR-guided adaptive radiation therapy (SMART) for pancreatic cancer. *Radiother Oncol*. 2017;125(3):439-444. doi:10.1016/j.radonc.2017.07.028
23. Acharya S, Fischer-Valuck BW, Kashani R, et al. Online magnetic resonance image guided adaptive radiation therapy: first clinical applications. *Int J Radiat Oncol*. 2016;94(2):394-403. doi:10.1016/j.ijrobp.2015.10.015
24. Mislow JMK, Golby AJ, Black PM. Origins of intraoperative MRI. *Magn Reson Imaging Clin N Am*. 2010;18(1):1-10. doi:10.1016/j.mric.2009.09.001
25. Tropp J. The theory of the bird-cage resonator. *J Magn Reson 1969*. 1989;82(1):51-62. doi:10.1016/0022-2364(89)90164-9
26. Hayes CE, Edelstein WA, Schenck JF, Mueller OM, Eash M. An efficient, highly homogeneous radiofrequency coil for whole-body NMR imaging at 1.5T. *Magn Reson Med*. 1985;63:622-628.
27. Dietrich KA, Klüter S, Debus J, et al. Construction of a Tx/Rx body coil on a rotatable patient capsule for MR-guided particle therapy. *Proc Intl Soc Mag Reson Med*. 2022;30:1094. London, England, Abstract.
28. Diaham S, O'Sullivan L, Ceccarelli E, et al. Improving polyimide isolation performance by tailoring interfaces with nitride layers for digital isolator application. *2020 IEEE 3rd Int Conf Dielectr ICD*. 2020:570-573. doi:10.1109/ICD46958.2020.9341967. Published online July.
29. Hoult DI, Chen CN, Sank VJ. Quadrature detection in the laboratory frame. *Magn Reson Med*. 1984;1(3):339-353. doi:10.1002/mrm.1910010305
30. Seeber DA, Jevtic J, Menon A. Floating shield current suppression trap. *Concepts Magn Reson Part B Magn Reson Eng*. 2004;21B(1):26-31. doi:10.1002/cmr.b.20008
31. Berger MJ, Coursey JS, Zucker MA, Chang J. Stopping-power & range tables for electrons, protons, and helium ions. *NIST*. 2023. Accessed March 20. https://www.nist.gov/pml/stopping-power-range-tables-electrons-protons-and-helium-ions. Published online October 7, 2009.
32. Bloch F. Zur Bremsung rasch bewegter Teilchen beim Durchgang durch Materie. *Ann Phys*. 1933;408(3):285-320. doi:10.1002/andp.19334080303
33. Levet A, Özdemir Y. Determination of effective atomic numbers, effective electrons numbers, total atomic cross-sections and buildup factor of some compounds for different radiation sources. *Radiation Physics and Chemistry*. 2017;130:171-176. doi:10.1016/j.radphyschem.2016.08.015
34. Platt T, Umathum R, Fiedler TM, et al. In vivo self-gated 23Na MRI at 7 T using an oval-shaped body resonator. *Magn Reson Med*. 2018;80(3):1005-1019. doi:10.1002/mrm.27103
35. Christ A, Kainz W, Hahn EG, et al. The Virtual Family—development of surface-based anatomical models of two adults and two children for dosimetric simulations. *Phys Med Biol*. 2009;55(2):N23. doi:10.1088/0031-9155/55/2/N01
36. Hasgall PA, Di Gennaro F, Baumgartner C, et al. IT'IS Database for thermal and electromagnetic parameters of biological tissues. 2022, Version 4.1. doi:10.13099/VIP21000-04-1
37. Dietrich KA, et al. Performance of a rotatable Tx/Rx body coil for MR-guided particle therapy. *Proc Intl Soc Mag Reson Med*. 2023;31:4385. Toronto, Canada, Abstract.
38. Insko EK, Bolinger L. Mapping of the radiofrequency field. *J Magn Reson A*. 1993;103(1):82-85. doi:10.1006/jmra.1993.1133
39. Determination of Signal-to-Noise Ratio (SNR) in Diagnostic Magnetic Resonance Imaging. NEMA. Published April 30, 2015. Accessed July 26, 2023. https://www.nema.org/standards/view/Determination-of-Signal-to-Noise-Ratio-in-Diagnostic-Magnetic-Resonance-Imaging
40. Vaidya MV, Collins CM, Sodickson DK, Brown R, Wiggins GC, Lattanzi R. Dependence of and field patterns of surface coils on the electrical properties of the sample and the MR operating frequency. *Concepts Magn Reson Part B Magn Reson Eng*. 2016;46(1):25-40. doi:10.1002/cmr.b.21319
41. Cloos MA, Knoll F, Zhao T, et al. Multiparametric imaging with heterogeneous radiofrequency fields. *Nat Commun*. 2016;7(1):12445. doi:10.1038/ncomms12445

42. Hoogcarspel SJ, Crijns SPM, Lagendijk JJW, van VulpenM, Raaymakers BW. The feasibility of using a conventional flexible RF coil for an online MR-guided radiotherapy treatment. *Phys Med Biol*. 2013;58(6):1925. doi:10.1088/0031-9155/58/6/1925
43. Barta R, Volotovskyy V, Wachowicz K, Fallone BG, De Zanche N. How thin can you go? Performance of thin copper and aluminum RF coil conductors. *Magn Reson Med*. 2021;85(4):2327-2333. doi:10.1002/mrm.28540
44. Liney GP, Dong B, Weber E, et al. Imaging performance of a dedicated radiation transparent RF coil on a 1.0 Tesla inline MRI-linac. *Phys Med Biol*. 2018;63(13):135005. doi:10.1088/1361-6560/aac813
45. Burke B, Fallone BG, Rathee S. Radiation induced currents in MRI RF coils: application to linac/MRI integration. *Phys Med Biol*. 2010;55(3):735. doi:10.1088/0031-9155/55/3/013
46. Burke B, Wachowicz K, Fallone BG, Rathee S. Effect of radiation induced current on the quality of MR images in an integrated linac-MR system. *Med Phys*. 2012;39(10):6139-6147. doi:10.1118/1.4752422
47. Marteau TM, Bekker H. The development of a six-item short-form of the state scale of the Spielberger State—Trait Anxiety Inventory (STAI). *Br J Clin Psychol*. 1992;31(3):301-306. doi:10.1111/j.2044-8260.1992.tb00997.x
48. Radomsky AS, Rachman S, Thordarson DS, McIsaac HK, Teachman BA. The claustrophobia questionnaire. *J Anxiety Disord*. 2001;15(4):287-297. doi:10.1016/S0887-6185(01)00064-0
49. Keshavarz B, Hecht H. Validating an efficient method to quantify motion sickness. *Hum Factors*. 2011;53(4):415-426. doi:10.1177/0018720811403736

SUPPORTING INFORMATION

Additional supporting information can be found online in the Supporting Information section at the end of this article.

How to cite this article: Dietrich KA, Klüter S, Dinkel F, et al. An essentially radiation-transparent body coil integrated with a patient rotation system for MR-guided particle therapy. *Med Phys*. 2024;51:4028–4043. https://doi.org/10.1002/mp.17065